scientific reports

Check for updates

OPEN

Hydrothermal synthesis of novel 1-aminoperylene diimide/TiO_2/MoS_2 composite with enhanced photocatalytic activity

Yongshan Ma[1]✉, Yue Wang[2], Tianyi Jiang[1], Fengxia Zhang[1]✉, Xuemei Li[1] & Yanyan Zhu[1]

1-aminoperylene diimide/TiO_2/MoS_2 composite (NH_2-PDI/TiO_2/MoS_2) with ordered structure was prepared by hydrothermal synthesis method. The composite was characterized by XRD, SEM, FTIR, XPS, BET, DRS, PL, EIS, Raman, photocurrent, and Mott-Schottky plots spectroscopy. The potential positions of the conduction and valence bands, and the band gap energy of the semiconductors were estimated. The composite exhibited higher photocatalytic activity compared with the mono-component systems. The apparent rate constants (k) were determined as 0.00616, 0.00352, 0.00738, 0.00517, 0.00752, and 0.00806 min^{-1} for TiO_2, NH_2-PDI, NH_2-PDI/TiO_2, MoS_2, MoS_2/TiO_2, and NH_2-PDI/TiO_2/MoS_2, respectively. The detection of radical scavengers confirmed that superoxide radicals, photogenerated holes, and photogenerated electrons were the main active substances for MB degradation. Between type II- heterojunction mechanism and Z-scheme mechanism, the latter could explain the enhanced photocatalytic activity of the composite better. The Z-scheme mechanism accumulates more electrons at CB level of NH_2-PDI and hence generates more super oxide radicals.

Water pollution is an important issue of concern in many countries. Many dyes in textile printing or dyeing wastewater contain aromatic compounds, which are chemically stable and harmful to human health[1]. Because of the adverse environmental impacts of these refractory organic compounds, it is necessary to develop new methods to degrade them. Photocatalysis is a promising technique for photodegradation of hazardous chemicals in wastewater[2]. Titanium dioxide (TiO_2) and TiO_2 based nanostructures are being used for photocatalytic degradation of organic pollutants to protect environment[3]. With the advantages of low cost, large specific surface area, high oxidizing power, and good chemical stability, TiO_2 has become one of the most promising candidates for photocatalysis[4]. However, the catalytic performance of TiO_2 is severely limited by the large band gap (3.2 eV), low photon utilization rate of solar energy (about 5%), and high recombination rate for photogenerated electron–hole pairs[5,6]. On the other hand, the industrial treatment of wastewater containing various organic pollutants using TiO_2-photocatalyst is not common due to low efficiency of photodegradation[7]. To solve this problem, several methods have been used to improve the photocatalytic efficiency of TiO_2. It has been reported that in a suitable heterostructured system, the presence of heterojunction changes the energy band positions and their inclination on the interface to accelerate the migration of photogenerated charge carriers, and eventually enhance the efficiency of photocatalyst[8].

Perylenetetracarboxylic acid diimides (PDIs) are cheap organic dyes with high photothermal stability and strong absorption in the visible region[9,10]. As a typical n-type semiconductor, PDIs have high electron mobility and electron affinity [LUMO] due to its strong π–π stacking between the conjugated π bonds[11,12]. PDIs materials have been used in photocatalysis because it can improve the light absorption and decrease the photo-generated electron–hole recombination[13]. PDIs have been introduced into TiO_2, ZnO, and other photocatalysts to improve the photocatalytic performance[14,15]. However, such composite materials still have some defects such as quick recombination of photoexcited electron–hole pairs and photoetching, which lead to low efficiency of visible light driven photodegradation[16]. Therefore, it is necessary to further improve their photocatalytic activities and stabilities.

[1]School of Municipal and Environmental Engineering, Shandong Jianzhu University, Shandong 250101, People's Republic of China. [2]Shandong Provincial Key Laboratory of Metrology and Measurement, Shandong Social Justice Institute of Metrology, Shandong Institute of Metrology, Jinan 250014, People's Republic of China. ✉email: mlosh@sdjzu.edu.cn; zhangfengxia19@sdjzu.edu.cn

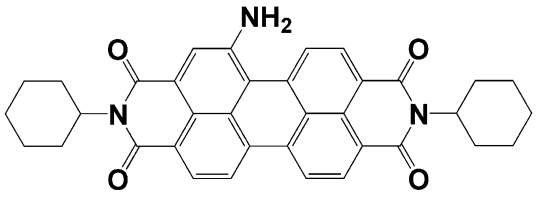

NH_2-PDI

Scheme 1. Molecular structure of 1-aminoperylene diimide (NH_2-PDI).

Molybdenum disulfide (MoS_2) is a rapidly rising two-dimensional layered material, which has aroused enormous scientific interest in developing new MoS_2-based materials for rich potential applications[17]. MoS_2 with different structures such as nanoribbon and nanosheet has been successfully synthesized[18,19]. It has unique physical properties that distinguish it from other materials and has been used in many applications such as lubricant, photovoltaic, and photocatalysis[20,21]. Hu et al. synthesized bulk, nano-slice, and nano-ball MoS_2 by precipitation method, and found that the photocatalytic efficiency of nano-slice MoS_2 towards methyl orange (90%) was higher than others[22]. James et al. synthesized MoS_2 nanoparticles through thermally decomposing method, and the material was used for photocatalytic degradation of methylene blue (MB) with an efficiency of 30%[23]. Xu et al. prepared flower-like MoS_2 nanopowders through hydrothermal method for photocatalytic degradation of Rhodamine B (RhB) and an efficiency of 15% was achieved[24]. In addition, the good conductivity of monolayer MoS_2 can efficiently separate the electron–hole pairs and enhance the photocatalytic activity. Hence, MoS_2 can be used in TiO_2 photocatalyst to improve its photocatalytic performance. For instance, Behzad Pourabbas et al. reported the photo-oxidation of phenol by MoS_2/TiO_2 hybrids. Suddhasatwa Basu et al. demonstrated the ability to degrade RhB by MoS_2/TiO_2 nanocomposite[25]. Giri et al. reported the photo-oxidation of RhB by MoS_2/TiO_2 hybrids[26]. Du et al. reported a $MoS_2/CdS/TiO_2$ photocatalyst which has high photocatalytic activity and stability[27]. This technique produces powerful non-selective oxidants, such as superoxide radicals and hydroxyl radicals, which can degrade and mineralize a wide variety of pollutants[28]. The produced electrons-holes would recombine in pure TiO_2, which limited its application in the photodegradation. By preventing electron/hole recombination and semiconductors aggregation, multi-component support can improve the photoreactivity of the obtained composite[29].

In this work, a novel ternary photocatalyst: NH_2-PDI/TiO_2/MoS_2 was synthesized by hydrothermal method (Scheme 1). The CB/VB (conduction band/valence band) of TiO_2, NH_2-PDI, and MoS_2 are evaluated to be − 1.26/1.72 eV, − 1.56/0.8 eV, and -0.75/1.00 eV, respectively. These matched potentials are suitable for rapid charge separation between these semiconductors. The composite showed enhanced activity in the photodegradation of Methylene Blue (MB) and amoxicillin (AMX).

Experimental

Materials and methods. All other chemicals were analytically pure, purchased from commercial sources and used without further purification. Distilled water was used throughout the experiment. FT-IR spectrum has been studied by a Bruker Tensor-27 spectrophotometer. The ^{1}H NMR and mass spectrum of NH_2-PDI were measured on a Bruker Advance 400 spectrometer and a Bruker Maxis UHR-TOF mass spectrometer, respectively. Scanning electron microscopy (SEM) images were obtained on a Sigma, Zeiss microscope equipped with an energy dispersive X-ray (EDX) spectrometer. The specific surface area of the catalyst has been analyzed using nitrogen adsorption at 77 K applying the Brunauer–Emmett–Teller (BET) method using a micrometrics ASAP 2020 V3.00 H. X-ray diffraction (XRD) measurements have been performed using a Rigaku R-AXIS RAPID X-ray diffractometer. Crystallinity and phase composition of the as-synthesized composite have been confirmed from the Lab Ram HR800, Jobin Yvon micro-Raman measurement. The ultraviolet–visible diffuse reflectance absorption spectra (DRS) have been measured on a Shimadzu model UV–Vis diffuse reflectance spectrometer. X-ray photoelectron spectroscopy (XPS) has been performed on a KRATOS model XSAM800 instrument. Fluorescence measurements were performed at a Hitachi FL-4500 spectrometer with 290 nm excitation wavelength at room temperature. The Mott-Schottky plots, photocurrent, and electrochemical impedance spectroscopy (EIS) were measured on a CHI760E electrochemical workstation using a three-electrode system. Platinum wire as counter electrode, ITO deposited by photocatalyst was used as working electrodes (50 mg of photocatalyst was dispersed in 2 mL of ethanol and grounded for 20 min, then it was uniformly dropped onto the FTO glass and stay still overnight to dry off the ethanol.), saturated calomel as reference electrode, and 0.1 M Na_2SO_4 aqueous solution was used as electrolyte. The EIS was performed at an open circuit potential at a frequency of 0–10,000 Hz, and the photoelectric response of the sample was measured at 0.0 V. Photoelectrochemical properties were measured with a 300 W xenon lamp as the light source.

Synthesis and characterization of NH_2-PDI. The compound NH_2-PDI was synthesized according to literature method[30]. The synthetic route along with the characterization data of NH_2-PDI (Fig. S-1) are reported in the Supplementary Methods.

Preparation of TiO_2 and NH_2-PDI/TiO_2. The NH_2-PDI/TiO_2 composite was prepared by the hydrothermal synthesis method. First, tetrabutyl titanate (10.0 mL) was dissolved in anhydrous ethanol (20.0 mL). Then, 5.0 mL of distilled water was slowly added under vigorous stirring. Later, NH_2-PDI (0.01 g) was dissolved in dichloromethane (5.0 mL) and added to the solution under sonication. The resulting mixture was stirred for 12 h and then transfer to the hydrothermal kettle for 3 h at 200 °C. The precipitate was filtered, washed thoroughly with distilled water, and dried in an air oven at 100 °C for 4 h. This catalyst contained 0.1 wt% of NH_2-PDI. Pure TiO_2 was prepared by the same method.

Preparation of MoS_2. MoS_2 was synthesized by hydrothermal route using $Na_2MoO_4{\cdot}2H_2O$ and NH_2CSNH_2 as Mo and S sources, respectively. Briefly, $Na_2MoO_4{\cdot}2H_2O$ (2.0 g) and NH_2CSNH_2 (8.0 g) was dissolved in 60 mL of water under vigorous stirring for 30 min. The mixture was kept in a hydrothermal kettle at 200 °C for 24 h. The resulting black precipitate was washed several times with ethanol and water to further remove impurities and contaminants followed by a centrifugation and drying process at 60 °C for 6 h to obtain MoS_2 nanoarchitectures.

Preparation of MoS_2/TiO_2 and NH_2-PDI/TiO_2/MoS_2. The NH_2-PDI/TiO_2/MoS_2 composite was fabricated by loading MoS_2 onto the preformed NH_2-PDI/TiO_2 solid solutions. Hydrothermal synthesis of NH_2-PDI/TiO_2/MoS_2 composite was prepared as follows: 3.0 g NH_2-PDI/TiO_2 and 0.06 g of MoS_2 were dispersed in 5 mL water. The resulting mixture was stirred for 24 h and then transferred to a hydrothermal kettle at 200 °C for 4 h. The prepared composite material was filtered, washed thoroughly with distilled water, and dried in an air oven at 100 °C for 4 h. NH_2-PDI/TiO_2/MoS_2 was formed as a gray powder. This catalyst contained 0.1 wt% NH_2-PDI and 2.0 wt% MoS_2. MoS_2/TiO_2, NH_2-PDI/TiO_2/1%MoS_2, and NH_2-PDI/TiO_2/3%MoS_2 were prepared using the same procedure.

Photocatalytic activity tests. The photocatalytic experiments were carried out in a photochemical reactor (PhchemIII, Beijing China NBeT) consisting of a 500 W xenon lamp (XE-JY500). The reaction chamber is equipped with 50 mL capacity reaction glass tubes and a magnetic stirrer. The specially designed reflector was made of highly polished aluminum and a built-in cooling fan. The light exposure length is 230 mm.

Methylene Blue (MB) and amoxicillin (AMX) were selected to test the photodegradation activity of the prepared photocatalysts. First, 50 mg of synthesized sample was suspended in 50 ml of 10 mg/L MB aqueous solution. The visible light source was obtained by a 500 W xenon lamp. Before irradiation, the suspension solutions were stirred magnetically for 120 min in the dark to achieve adsorption–desorption equilibrium. The samples were withdrawn at given time intervals and the photocatalyst was removed by centrifugation. A UV–vis spectrophotometer at 664 nm and 198 nm was used to measure the absorbance of MB and AMX solutions, respectivly.

Results and discussion

Figure 1 shows SEM images of TiO_2, NH_2-PDI, NH_2-PDI/TiO_2, MoS_2, MoS_2/TiO_2, and NH_2-PDI/TiO_2/MoS_2. Figure 1(a) shows that TiO_2 forms uniform elongated spherical particles with a length of about 300 nm and a width of about 200 nm. As can be seen from Fig. 1(b), NH_2-PDI forms nanorods structure. The average width is 1 μm, and the length is in the range of 1–3 μm. Figure 1(c) depicts that NH_2-PDI/TiO_2 particles formed an agglomerated spherical structure. As shown in Fig. 1d, the average diameter of MoS_2 nanoflowers is 0.5–1 μm. These nanoflowers have massive petals on the surfaces, which are free to gather closely. Figure 1(e) and (f) shows the morphology of the synthesized MoS_2/TiO_2 heterostructure characterized by SEM. It can be seen that MoS_2 and TiO_2 mixed together. In Fig. 1(h) and (i), a peculiar morphology of NH_2-PDI/TiO_2/MoS_2 is shown. The NH_2-PDI and MoS_2 mixed with TiO_2, and they can provide more active sites and mass charge transport pathways in the catalytic system. The color of MoS_2/TiO_2 and NH_2-PDI/TiO_2/MoS_2 are shown in Fig. 1(g) and (j), respectively. MoS_2/TiO_2 was light grey while NH_2-PDI/TiO_2/MoS_2 sample showed a red grey color.

The composition of the NH_2-PDI/TiO_2/MoS_2 was further investigated by an EDX attached to SEM (Fig. 2). Figure 2(b)–(h) shows the element mappings in a selected area of the composite (Fig. 2a). The homogeneous distributions of the elements Mo, S, C, N, Ti, and O can be clearly seen from the graphs. As shown in Fig. 2(i) and Fig. S-2, EDX analysis reveals that the composite contains Ti and O (in the case of TiO_2), Mo and S (in the case of MoS_2), or C and N (in the case of NH_2-PDI). The atomic ratio of Ti, Mo and C equals to 25.2: 1: 1.3, meaning that the molar ratio of TiO_2, MoS_2, and NH_2-PDI is about 95.3: 1.89: 0.68. The high proportion of C is due to the elemental carbon and carbonate species adsorbed on the TiO_2 surface.

XRD measurements were performed to determine the crystalline structures of TiO_2, NH_2-PDI, NH_2-PDI/TiO_2, MoS_2, MoS_2/TiO_2, and NH_2-PDI/TiO_2/MoS_2 composites (Fig. 3). The crystal phase of TiO_2 was consistent with anatase phase TiO_2 (JCPDS NO. 71–1167) (Fig. 3a). Diffraction peaks appeared at $2\theta = 25.3°$, 37.7°, 48.0°, 53.8°, 55.0°, 62.6°, 58.6°, 70.6°, and 75.2°, corresponding to (101), (311), (200), (105), (211), (204), (116), (220), and (241) planes of TiO_2, respectively[31]. The NH_2-PDI appeared in the corresponding d-spacing as 10.35 Å, 9.22 Å, 5.24 Å, and 3.43 Å (Fig. 3b). The peak at $2\theta = 25.74°$ (*d* spacing 3.43 Å) can be attributed to the π-π stacking of the adjacent NH_2-PDI, since the distance of π-π stacking between the perylene nuclei was about 3.5 Å[32]. It was well known that PDIs exhibit a typical sharp diffraction peak at about 8–9°, which was centered at 9.57° (*d* spacing 9.22 Å)[33]. Additionally, X-ray powder diffraction measurements on NH_2-PDI showed that the first diffraction peak appeared at $2\theta = 8.53°$ (*d* spacing 10.35 Å) and the second-order diffraction peak appeared at $2\theta = 16.85°$ (*d* spacing 5.24 Å). The first diffraction peak was assigned as (001) and the second peak was assigned as (002) α-form crystal diffraction, which has been reported by Miyata[34]. The multiple orders of reflection indicated that the self-assembled structures of NH_2-PDI are well-ordered and layered microstructures. For the pure 3D flower-like spherical MoS_2 nanostructure, the peaks correspond to (002), (100), (103), and (110) diffraction planes of 2H-MoS_2 (JCPDS: 37-1492), which is consistent with previous studies (Fig. 3d)[35]. For MoS_2/TiO_2, the

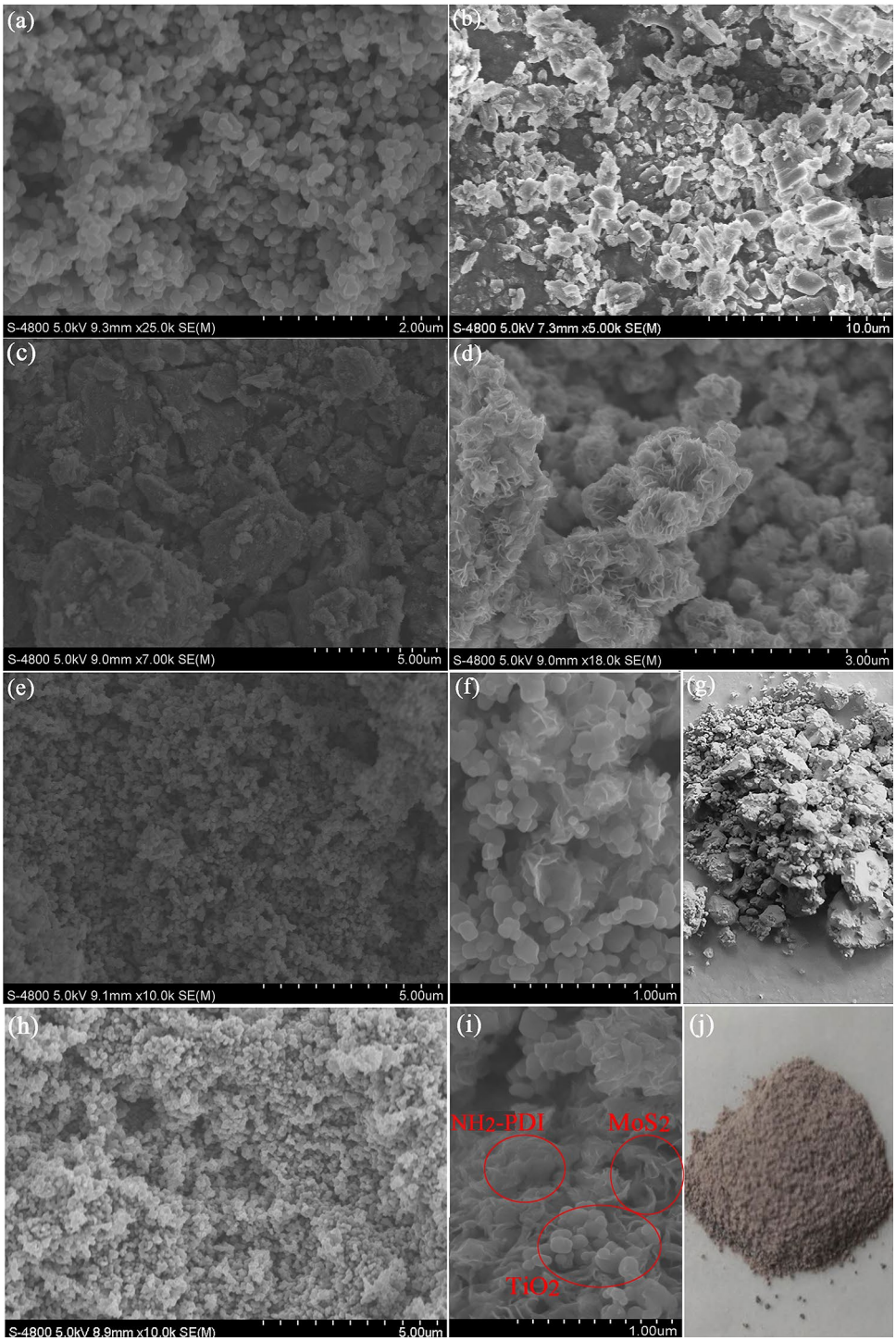

Figure 1. SEM images of TiO_2 (**a**), NH_2-PDI (**b**), NH_2-PDI/TiO_2 (**c**), MoS_2 (**d**), MoS_2/TiO_2 (**e**,**f**), NH_2-PDI/TiO_2/MoS_2 (**h**,**i**), and the appearance of MoS_2/TiO_2 (**g**), NH_2-PDI/TiO_2/MoS_2 (**j**).

addition of MoS_2 did not change the diffraction peak positions of TiO_2 obviously, indicating that MoS_2 was not incorporated into the TiO_2 lattice. Obviously, both NH_2-PDI/TiO_2 and NH_2-PDI/TiO_2/MoS_2 formed ordered structures. Comparison of the XRD patterns in Fig. 3a,c,e,f confirms that the XRD patterns of the NH_2-PDI/TiO_2, MoS_2/TiO_2, and NH_2-PDI/TiO_2/MoS_2 nanoparticles have good consistency with the XRD data of anatase phase TiO_2 (JCPDS NO. 71–1167) at 2θ degrees of 25.3°, 37.7°, 48.0°, 53.8°, 55.0°, 62.6°, 58.6°, 70.6°, and 75.2°[36]. Compare with pure TiO_2, the crystallization properties of the two composites were slightly weakened, which should be due to the binding of NH_2-PDI (Fig. 3c,f). Since the NH_2-PDI/TiO_2/MoS_2 composite was loaded with very little NH_2-PDI and MoS_2, the characteristic peaks of NH_2-PDI and MoS_2 did not appear in its XRD patterns (Fig. 3f). Additionally, compared with pure TiO_2, NH_2-PDI/TiO_2/MoS_2 exhibited a widened peak width. This

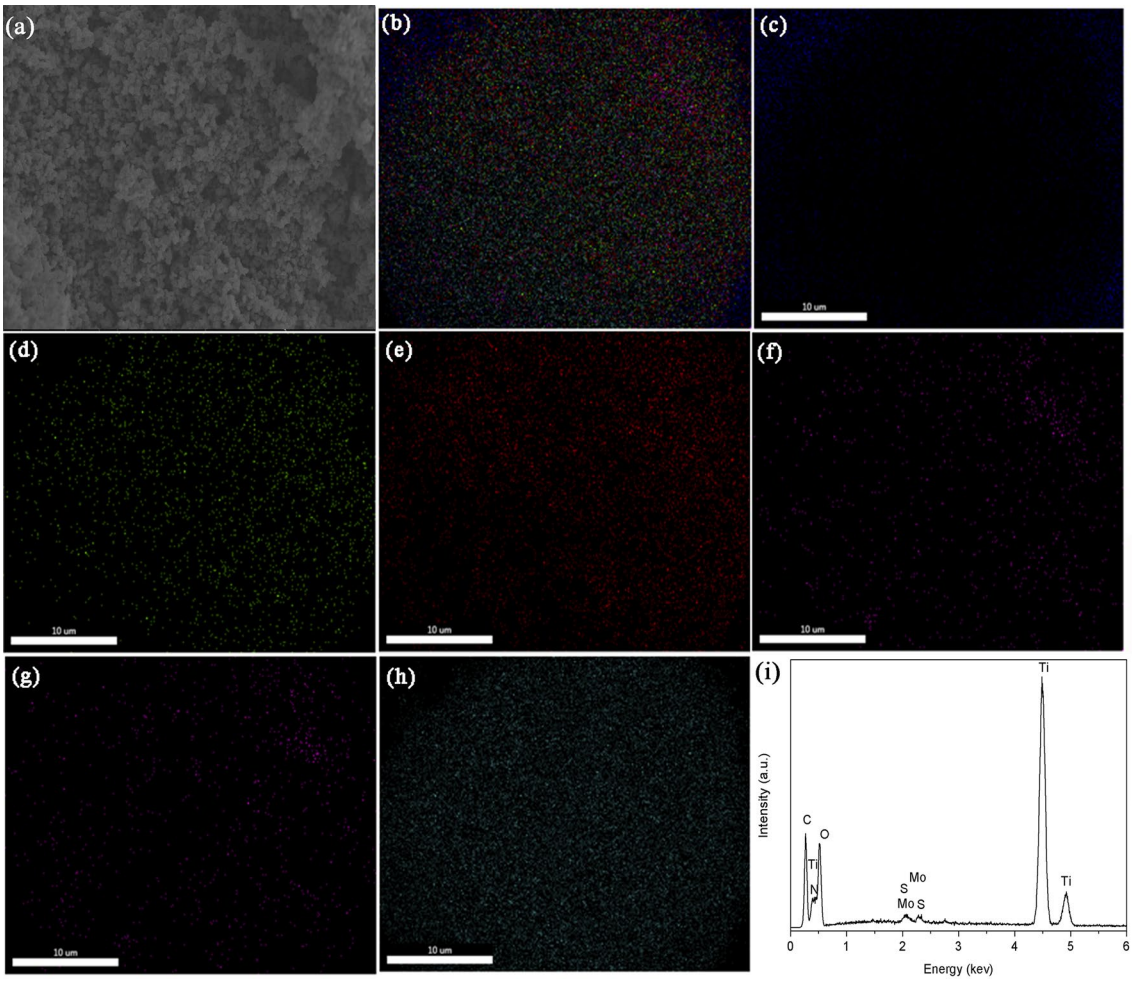

Figure 2. (**a**) SEM image of NH_2-PDI/TiO_2/MoS_2 photocatalyst; Element mappings of Mo, S, C, N, Ti, and O elements (**b**), C (**c**), N (**d**), O (**e**), Mo (**f**), S (**g**), and Ti (**h**) in the NH_2-PDI/TiO_2/MoS_2 photocatalyst; (**i**) EDX spectrum of NH_2-PDI/TiO_2/MoS_2 photocatalyst.

may be caused by the formation of heterojunction between TiO_2, NH_2-PDI and MoS_2, and the heterojunction lead to lattice distortion of TiO_2. The average particle sizes of TiO_2, NH_2-PDI/TiO_2, MoS_2/TiO_2, and NH_2-PDI/TiO_2/MoS_2 calculated by Scherrer's equation were 10.2 nm, 12.5 nm, 11.3 nm, and 13.6 nm, respectively[37].

Raman spectroscopy was applied to further check the phase and formation of the NH_2-PDI/TiO_2/MoS_2 nanocomposite. As shown in Fig. S-3, the pristine TiO_2 nanoparticles exhibit five peaks at 145.1 ± 0.2, 196.6 ± 0.1, 396.1 ± 0.2, 513.7 ± 0.2, and 638.1 ± 0.1 cm^{-1}, which belong to the E_g, E_g, B_{1g}, A_{1g}, and E_g anatase tetragonal vibration modes of TiO_2, respectively[38]. The E_g, B_{1g}, and A_{1g} peaks correspond to symmetric stretching, symmetric bending, and antisymmetric bending vibrations of O-Ti–O, respectively. The results demonstrate the existence of typical anatase TiO_2 phase, and it is consistent with the XRD results. Characteristic peaks of MoS_2 (A_{1g} and E^1_{2g} modes) were observed in the Raman spectra of NH_2-PDI/TiO_2/MoS_2 photocatalyst, indicating that MoS_2 was loaded on the surface of TiO_2[39]. Compared with pure TiO_2, NH_2-PDI/TiO_2/MoS_2 photocatalyst exhibited red shifts of E_g, E_g, A_{1g}, and E_g modes (145.6 ± 0.3, 197.8 ± 0.1, 514.1 ± 0.1, and 638.4 ± 0.1 cm^{-1}). This indicates that there are strong intimate interactions between TiO_2, MoS_2, and NH_2-PDI.

FT-IR measurements revealed the connection between TiO_2, NH_2-PDI and MoS_2 in NH_2-PDI/TiO_2/MoS_2 nanocomposite (Fig. S-4). As shown in Fig. S-4a, for pure TiO_2, the vibration modes observed at 617 cm^{-1} and 749 cm^{-1} are due to the O–Ti–O bending and Ti–O stretching vibrations, respectively. For MoS_2, the vibration mode at 1389 cm^{-1} is assigned to Mo–S vibration, while the vibration mode at 1550 cm^{-1} may be S–O asymmetric stretching (Fig. S-4d)[40]. In MoS_2/TiO_2 and NH_2-PDI/TiO_2/MoS_2, all characteristic vibration modes were present but with very low Mo–S and S–O vibration modes, which indicates that the MoS_2/TiO_2 and NH_2-PDI/TiO_2/MoS_2 contain very little amount of MoS_2 (Fig. S-4e, f). Remarkably, the bending vibration of C-H at 2926–2817 cm^{-1} observed in NH_2-PDI shifted to 2968–2875 cm^{-1} in NH_2-PDI/TiO_2 and to 2992–2889 cm^{-1} in NH_2-PDI/TiO_2/MoS_2, which may be an indicative of the binding between NH_2-PDI and TiO_2 or MoS_2. In addition, the stretching vibration of C = C in NH_2-PDI at 1645 cm^{-1} shifted to 1639 cm^{-1} in NH_2-PDI/TiO_2 and to 1627 cm^{-1} in NH_2-PDI/TiO_2/MoS_2 nanocomposite. Compared with NH_2-PDI, the C=C absorption peak of NH_2-PDI/TiO_2/MoS_2 was blue shifted, indicating that the π-π interaction within NH_2-PDI decreased. The absorption peak around 3300 cm^{-1} was caused by the stretching vibration of O–H bond, which was related to the atmospheric

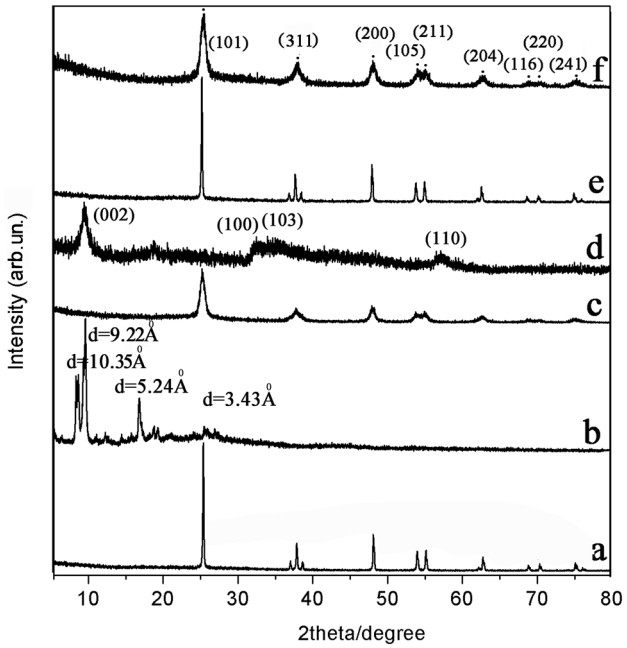

Figure 3. XRD patterns of TiO_2 (**a**), NH_2-PDI (**b**), NH_2-PDI/TiO_2 (**c**), MoS_2 (**d**), MoS_2/TiO_2 (**e**), NH_2-PDI/TiO_2/MoS_2 (**f**).

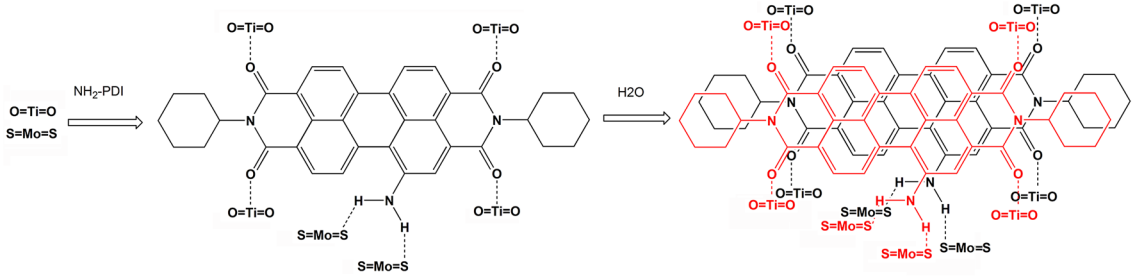

Figure 4. Graphical representation of the investigated adsorption mode of NH_2-PDI onto the TiO_2 and MoS_2 surface.

water adsorbed on the catalyst surface. As shown in Fig. 4, the Ti…O bond and S…H bond can be formed when NH_2-PDI meets with TiO_2 and MoS_2. After the addition of deionized water, NH_2-PDI self-assembled through intermolecular π–π stacking interactions. For NH_2-PDI, dichloromethane is a "good" solvent, while water is a "poor" solvent. When the "poor" solvent was added, the solubility of originally dissolved NH_2-PDI was limited, and NH_2-PDI self-assembled through non-covalent interactions and precipitated into solid.

The chemical composition and valence state of NH_2-PDI/TiO_2/MoS_2 sample were studied by XPS (Fig. 5). According to Fig. 5a, NH_2-PDI/TiO_2/MoS_2 composite contains Ti, O, C, Mo, and S elements. For NH_2-PDI/TiO_2/MoS_2 nanocomposite, the positions of Ti2p1/2 and Ti2p3/2 were observed at 464.9 eV and 459.1 eV, respectively. While for pure TiO_2 nanoparticles, Ti2p1/2 and Ti2p3/2 peaks were observed at 464.3 eV and 458.5 eV, respectively (Fig. 5b)[41]. The O1s peak positions of NH_2-PDI/TiO_2/MoS_2 and pure TiO_2 were observed at 530.2 eV and 529.8 eV, respectively (Fig. 5c). These results indicate that after adding NH_2-PDI and MoS_2 to TiO_2 nanoparticles, Ti2p peaks move to a higher energy by 0.6 eV than pure TiO_2. Also, the peak position of O1s moved 0.4 eV towards high energy. The shifted spectrum implies the presence of more defects or adsorbed hydroxyl groups on the surface of NH_2-PDI/TiO_2/MoS_2[42]. These defect states may serve as shallow donors to enhance charge transfer at the multiple interfaces and thus improve the overall degradation efficiency towards dyes. In NH_2-PDI/TiO_2/MoS_2 sample, The C1s spectra (Fig. 5d) shows the corresponding peak at 284.8 eV, which can be identified as C–C/C=C/C–H functional groups. The positions of the Mo3d5/2 and Mo3d3/2 peaks were observed at 232.4 eV and 228.5 eV, respectively. Similarly, the position of S2p was observed at 161.9 eV[43].

The surface areas of TiO_2, NH_2-PDI, NH_2-PDI/TiO_2, MoS_2, MoS_2/TiO_2, and NH_2-PDI/TiO_2/MoS_2 were determined by nitrogen adsorption method. The BET surface area of NH_2-PDI/TiO_2/MoS_2 (39 m^2/g) is higher than that of TiO_2 (21 m^2/g), NH_2-PDI/TiO_2 (37 m^2/g), MoS_2 (23 m^2/g), or MoS_2/TiO_2 (26 m^2/g). Therefore, it can be speculated that the large surface area of NH_2-PDI/TiO_2/MoS_2 could promote the photocatalytic activity.

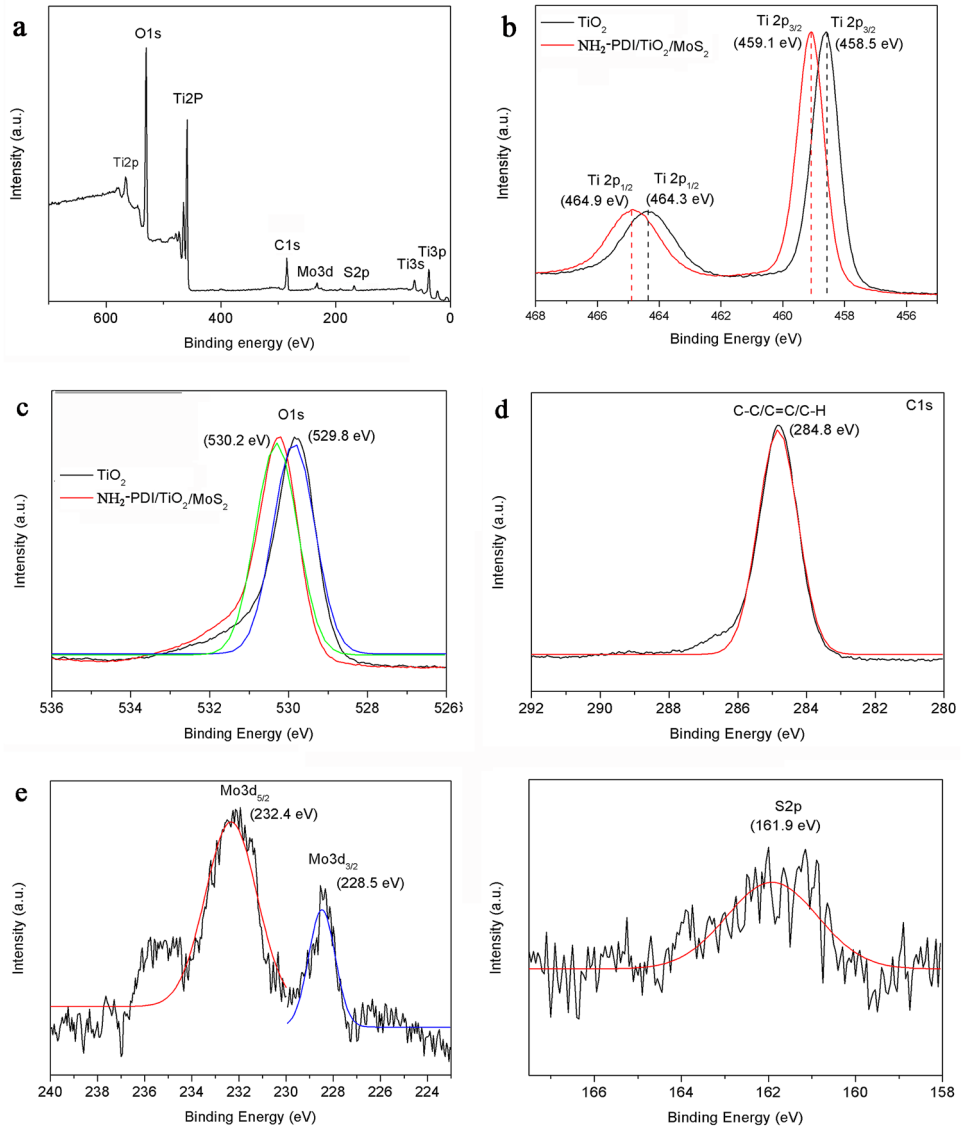

Figure 5. XPS spectra of (**a**) survey spectra in NH_2-PDI/TiO_2/MoS_2, (**b**) Ti2p in pure TiO_2 and NH_2-PDI/TiO_2/MoS_2, (**c**) O1s in pure TiO_2 and NH_2-PDI/TiO_2/MoS_2, (**d**) C1s in NH_2-PDI/TiO_2/MoS_2, (**e**) Mo3d in NH_2-PDI/TiO_2/MoS_2, and (**f**) S2p in NH_2-PDI/TiO_2/MoS_2.

The UV–vis diffuse reflection spectra (DRS) and the corresponding Tauc plots of samples are shown in Fig. 6. Pure TiO_2 absorbs only UV light and exhibits absorption below 380 nm. Adding NH_2-PDI and MoS_2 nanoflakes to TiO_2 nanoparticles can result in more light-harvesting in visible region (Fig. 6a). The absorption intensity of NH_2-PDI/TiO_2/MoS_2 in visible light region was obviously enhanced, which could be attributed to the visible light absorption characteristics of NH_2-PDI and MoS_2 nanoflakes. The band gap energy of the samples can be estimated by the formula Eg (eV) = 1240/λ_{AE} (nm) using the position of the absorption edge (λ_{AE})[44]. The downward slopes of the absorption curves are extrapolated to cross the X-axis and the λ_{AE}-values of TiO_2, MoS_2/TiO_2, NH_2-PDI/TiO_2, and NH_2-PDI/TiO_2/MoS_2 samples were estimated to be at 389 nm, 423 nm, 459 nm, and 467 nm, respectively (Fig. S-5). The Eg values of TiO_2, MoS_2/TiO_2, NH_2-PDI/TiO_2, and NH_2-PDI/TiO_2/MoS_2 samples were estimated to be at 3.18, 2.93, 2.70, and 2.66 eV, respectively.

The band gaps (Eg, eV) of the samples are also calculated by the Tauc equation and Kubelka–Munk function[45]:

$$[F(R)h\upsilon]^0.5 = A(h\upsilon - Eg) \quad (1)$$

$$F(R) = (1 - R)^2/2R \quad (2)$$

where, R is the calibrated reflection of samples with $BaSO_4$ reflection, and F(R) is proportional to the absorption constant. h and ν represent the Planck constant and frequency, while A and Eg represent constant and band gap

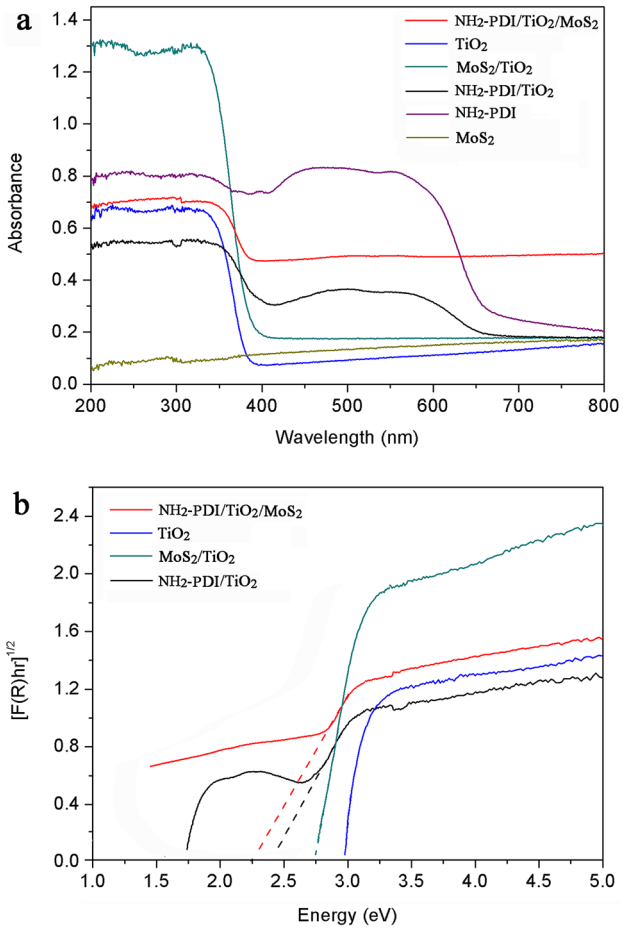

Figure 6. (**a**) UV–vis diffuse reflection spectra (DRS) and (**b**) The corresponding Tauc plot of samples.

energy, respectively. The $[F(R)hv]^{0.5}$ versus hν is shown in Fig. 6b. Extrapolation of the linear portion at $[F(R)hv]^{0.5} = 0$ provides Eg value of the samples. The band gaps were found to be 2.98, 2.75, 2.47, and 2.27 eV for TiO_2, MoS_2/TiO_2, NH_2-PDI/TiO_2, and NH_2-PDI/TiO_2/MoS_2, respectively. The increase of UV–visible light absorption and decrease of band gap energy enhanced the photodegradation efficiency of NH_2-PDI/TiO_2/MoS_2 towards MB.

The activity diagram of MB degradation by different catalysts in visible light and the first order kinetics curve fitting of MB degradation by different catalysts are shown in Fig. 7. Prior to the illumination, each catalyst was dispersed in the dye solution. After 120 min of vigorous magnetic stirring under dark condition, 51.3 ± 1.5% of MB was absorbed by NH_2-PDI/TiO_2/MoS_2, whereas pure TiO_2 only absorbed 8.2 ± 0.7% of MB. It can be seen that the spongy NH_2-PDI clusters and multi-layer MoS_2 nanoflowers decorated TiO_2 exhibited extremely high adsorption efficiency under dark condition. Both MoS_2 and TiO_2/MoS_2 have strong adsorption capacity, which may be due to the flower-like MoS_2 with negative surface charge promoted the adsorption of cationic dye MB. It can be noted that after 120 min of irradiation, the degradation rate of dye was 99.0 ± 1.0% for NH_2-PDI/TiO_2/MoS_2, while the corresponding data was 4.0 ± 0.3%, 31.3 ± 1.5%, 71.7 ± 1.6%, 78.7 ± 1.3%, and 87.6 ± 1.5% for NH_2-PDI, TiO_2, NH_2-PDI/TiO_2, MoS_2, and MoS_2/TiO_2, respectively (Fig. 7A). Though TiO_2 has no visible light absorption, it has been found to be solar active. This may be due to the dye sensitization mechanism of MB to TiO_2. For better comparison, NH_2-PDI/TiO_2/1%MoS_2 or NH_2-PDI/TiO_2/3%MoS_2 photocatalysts was used for dye degradation under identical conditions. As a result, 97.3 ± 0.6% or 94.0 ± 1.1% of dye were degraded respectively under visible light irradiation in 120 min. The results show that 0.1%NH_2-PDI/TiO_2/2%MoS_2 had higher efficiency in MB degradation than other catalysts. The kinetics plot shows that ln (C_0/C) has linear relationships with reaction time, indicating that the photodegradation of MB follows first-order kinetics (Fig. 7B). The apparent rate constants (k) were determined as 0.00616, 0.00352, 0.00738, 0.00517, 0.00752, and 0.00806 min^{-1} for TiO_2, NH_2-PDI, NH_2-PDI/TiO_2, MoS_2, MoS_2/TiO_2, and NH_2-PDI/TiO_2/MoS_2, respectively. These results confirmed the high photocatalytic activity of NH_2-PDI/TiO_2/MoS_2. Fig. S-6 shows the decolorization of MB dye (0.01 g/L) within 90 min in the presence of NH_2-PDI/TiO_2/MoS_2 catalyst. The decrease of absorption spectrum indicates decolorization of the dye under the applied conditions. There were no additional peaks in the UV–Vis spectrum, indicating that the dye was completely degraded. It is reported that the products of the decolorization process are H_2O, CO_2, NO_2, and SO_2[46], and the mechanism of MB degradation is shown in Fig. S-7.

Chemical oxygen demand (COD) is an indicator that reflecting the required oxygen for the oxidation of organic matters present in solution[47]. A smaller COD value means a lower pollution of the sample. The

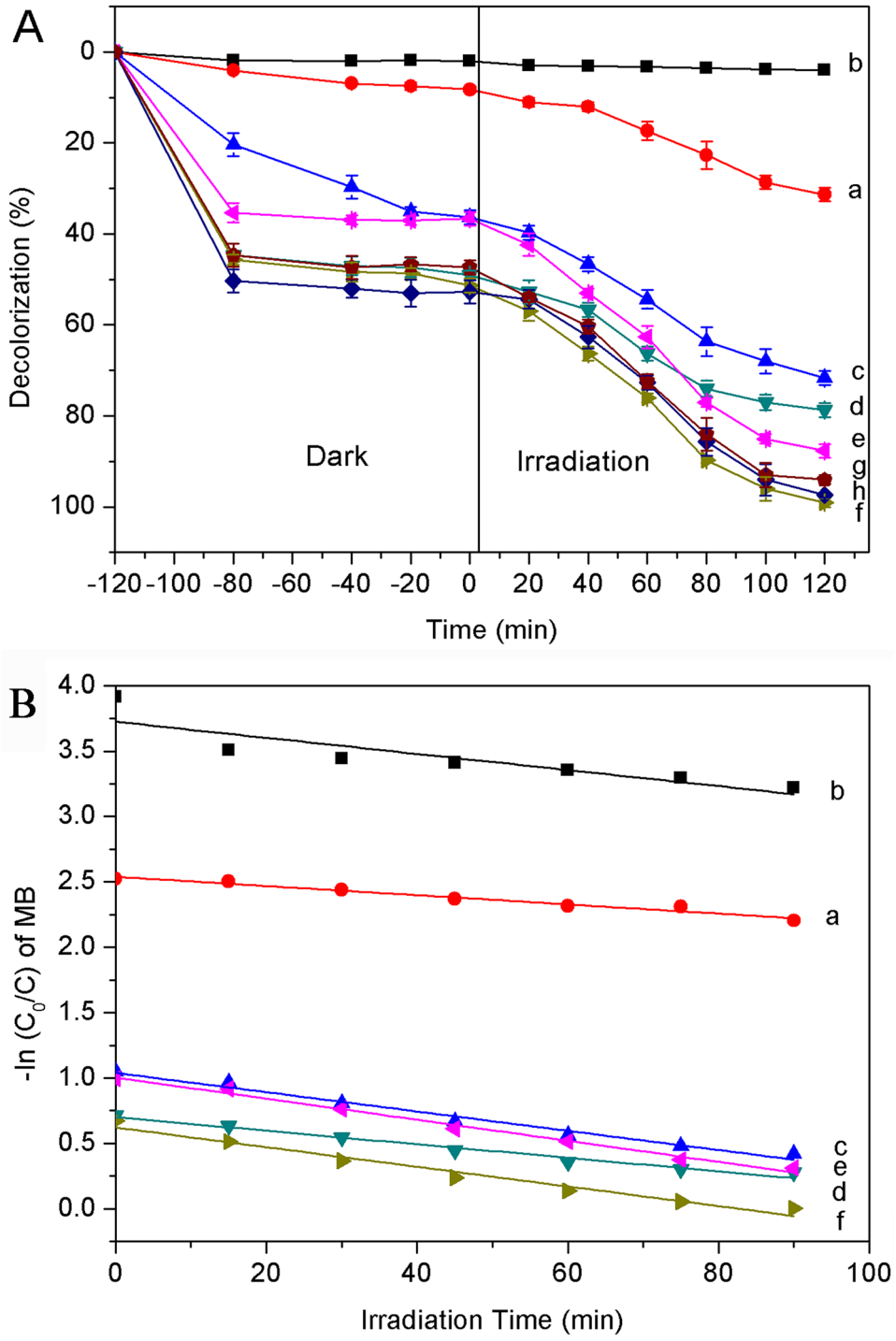

Figure 7. (**A**) The activity diagram of MB degradation by different catalysts in visible light, (**B**) The first order kinetics curve fitting of MB degradation by different catalysts. (a) TiO_2, (b) NH_2-PDI, (c) NH_2-PDI/TiO_2, (d) MoS_2, (e) MoS_2/TiO_2, (f) NH_2-PDI/TiO_2/2%MoS_2, (g) NH_2-PDI/TiO_2/1%MoS_2, and (h) NH_2-PDI/TiO_2/3%MoS_2. [MB] = 0.01 g/L, pH = 7, catalyst suspended = 1 g/L.

mineralization degree of MB was calculated by COD result, and the kinetic results shown that the k value of NH_2-PDI/TiO_2/MoS_2 was 0.0076 min^{-1} (Fig. S-8). The value correspond to $t_{1/2}$ values of 85.9 and 91.2 min (based on $t_{1/2} = 0.693/k$) for the degradation and mineralization of MB molecules, respectively[48]. These confirmed that the photodegradation of MB was 1.06 times faster than its mineralization. The results confirmed a relatively smaller mineralization extent for MB molecules than its photodegradation extent.

The photonic efficiency of MB dye degradation by NH_2-PDI/TiO_2/MoS_2 under optimum condition was calculated using a reported method[49]. The quantum yield of reaction (Ø) is defined as follows (Eq. (1)):

$$Ø = \frac{\text{Number of molecules decomposed}}{\text{Number of photons of light absorbed}}$$

The photo-degradation rate constants (k') of MB dyes under monochromatic light source can also be used to calculate the reaction quantum yield (Eq. (2)).

$$Ø = \frac{k'}{303I\varepsilon l}$$

where Ø is the reaction of quantum yield. I is the light intensity range in 400–800 nm (2.312×10^{-3} Einstein). ε is the molar absorptivity of MB at 664 nm (25,440 cm^{-1} M^{-1}). l is the path length of reaction tube, which is 0.23 m for 50 mL solution. The degradation quantum yields obtained with TiO_2, NH_2-PDI, NH_2-PDI/TiO_2, MoS_2, MoS_2/TiO_2, and NH_2-PDI/TiO_2/MoS_2 were 0.000152, 0.000869, 0.000182, 0.000128 and 0.000186, respectively. These results indicate that the quantum yield of NH_2-PDI/TiO_2/MoS_2 catalyzes process was higher than that of other processes.

During the process of MB degradation, a large amount of MB was adsorbed on the surface of catalysts. The visible light driven catalysis of the NH_2-PDI/TiO_2/MoS_2 may be enhanced due to the effect of dye sensitization. Therefore, amoxicillin (AMX, a colorless medical antibiotic) was selected to evaluate the photocatalytic activity of NH_2-PDI/TiO_2/MoS_2 nanoparticles under the same conditions. The photocatalytic degradation results of AMX are shown in Fig. S-9. NH_2-PDI/TiO_2/MoS_2 exhibited higher visible photocatalytic activity than NH_2-PDI/TiO_2 or MoS_2/TiO_2. When AMX solution was mixed with NH_2-PDI/TiO_2/MoS_2 in the absence of light, the removal rate of AMX was 48%. When NH_2-PDI/TiO_2 or MoS_2/TiO_2 was used under visible light irradiation for 120 min, the degradation rates of AMX were 56.9% or 71.2%, respectively. Comparatively, NH_2-PDI/TiO_2/MoS_2 exhibited superior photodegradation performance (84.8%). The degradation processes conforms to pseudo-first-order kinetics. The photocatalytic activity of NH_2-PDI/TiO_2/MoS_2 reached a maximum value of 0.00986 min^{-1}, which was about 1.67 times and 1.79 times higher than NH_2-PDI/TiO_2 and MoS_2/TiO_2 (0.00590 min^{-1} and 0.00551 min^{-1}), respectively. The result indicates that NH_2-PDI/TiO_2/MoS_2 has strong visible-light driven photocatalytic activity.

The reusability and stability of a composite photocatalyst are important factor affecting its application (Fig. S-10). The NH_2-PDI/TiO_2/MoS_2 was used for the degradation of different solutions of MB for six consecutive experiments under the same reaction conditions. After each experiment, the catalyst was recovered by centrifugation and dried in an air oven. The degradation efficiency of NH_2-PDI/TiO_2/MoS_2 reduced from 99 ± 0.9% to 89 ± 2.3% after six cycles of reuse, which was probably due to a small loss of catalyst during recycle (Fig. S-10a). NH_2-PDI/TiO_2/MoS_2 was prepared by hydrothermal synthesis method, which made the contact between three monomers more compacted and reduced the dissolution of MoS_2 or NH_2-PDI molecule. Therefore, the composite catalyst exhibits high stability in the degradation process. In addition, the composite material packaged TiO_2 by NH_2-PDI and MoS_2. The contact area between the three semiconductors increases due to the point-to-surface contact. Due to the close contact interface, the interactions between the three semiconductors would also be more intense. The π-conjugated electrons in NH_2-PDI can be quickly transferred from the interior of the semiconductor to the surface, and then to the surface of TiO_2 or MoS_2. This reduces electrons and holes recombination and improves the photocatalytic activity. Fig. S-10b shows the FT-IR spectra of the NH_2-PDI/TiO_2/MoS_2 photocatalyst before and after six cycles of photocatalytic degradation of MB. It can be seen that the spectrum of the regenerated photocatalyst was basically the same as that of the fresh photocatalyst. There is no spectrum of MB, which proves that MB has been completely degraded rather than adsorbed on the catalyst surface during the illumination process. The result of UV–vis spectra shows that the concentration of organic matter in the washing solution of catalyst was very low. Few intermediate species and NH_2-PDI were detected, indicating that the dissolution of NH_2-PDI in the composite structure was very few and MB was mineralized to CO_2. These results show that the NH_2-PDI/TiO_2/MoS_2 catalyst is stable and reusable.

The photoluminescence (PL) spectrum was used to analyze the recombination of electron hole pairs. In general, a higher peak indicates a more rapid charge recombination. As shown in Fig. S-11, the peak at 399 nm is attributed to a direct transition from the conduction band to the valence band. Moreover, the luminescence peaks at 440, 451, and 469 nm are caused by inter-band transitions, and the peaks at 483 and 492 nm are caused by intra-band transitions within the energy level traps or surface states[50]. The peak intensity was arranged as follow: TiO_2 > NH_2-PDI/TiO_2 > MoS_2/TiO_2 > NH_2-PDI/TiO_2/MoS_2. Especially, the peak intensity of NH_2-PDI/TiO_2/MoS_2 composite was much weaker than that of the pure TiO_2. The –C=O…H hydrogen bond between the -OH of TiO_2 and –C=O of NH_2-PDI, and the S…H bond between the -S of MoS_2 and -NH_2 of NH_2-PDI acted as short and fast channels for migrating the photogenerated charge carriers from NH_2-PDI to TiO_2 and MoS_2. Based on the above results, the introduction of NH_2-PDI and MoS_2 can greatly accelerate the charge transfer process.

The mechanism of enhanced photocatalytic activity of NH_2-PDI/TiO_2/MoS_2 composite was further studied by photoelectrochemistry method. The separation of photogenerated electrons and holes plays an important role in the photocatalytic decomposition of organic pollutants, which can be evaluated by transient photocurrent responses (I-t) and electrochemical impedance spectra (EIS) (Fig. 8). Figure 8a shows the I-t curves of TiO_2, NH_2-PDI, NH_2-PDI/TiO_2, MoS_2, MoS_2/TiO_2, and NH_2-PDI/TiO_2/MoS_2 under several intermittent visible light irradiation cycles. It can be seen that the photocurrent of all samples exhibited good repeatability when the light was turned on and off. The light current response of pure TiO_2 and NH_2-PDI were very weak (only 0.119 and 0.035 μA cm^{-2}, respectively). NH_2-PDI/TiO_2/MoS_2 composite had the largest photocurrent response, and the stable photocurrent was about 1.007 μA cm^{-2}, which was higher than that of MoS_2 (0.372 μA cm^{-2}), MoS_2/TiO_2 (0.522 μA cm^{-2}), and NH_2-PDI/TiO_2 (0.846 μA cm^{-2}). The enhanced photocurrent response indicates that the separation efficiency of photogenerated carriers and the photocatalytic performance were improved. Figure 8b displays the EIS Nyquist plots of as-prepared samples. The radius of the arc on the EIS spectrum reflects the

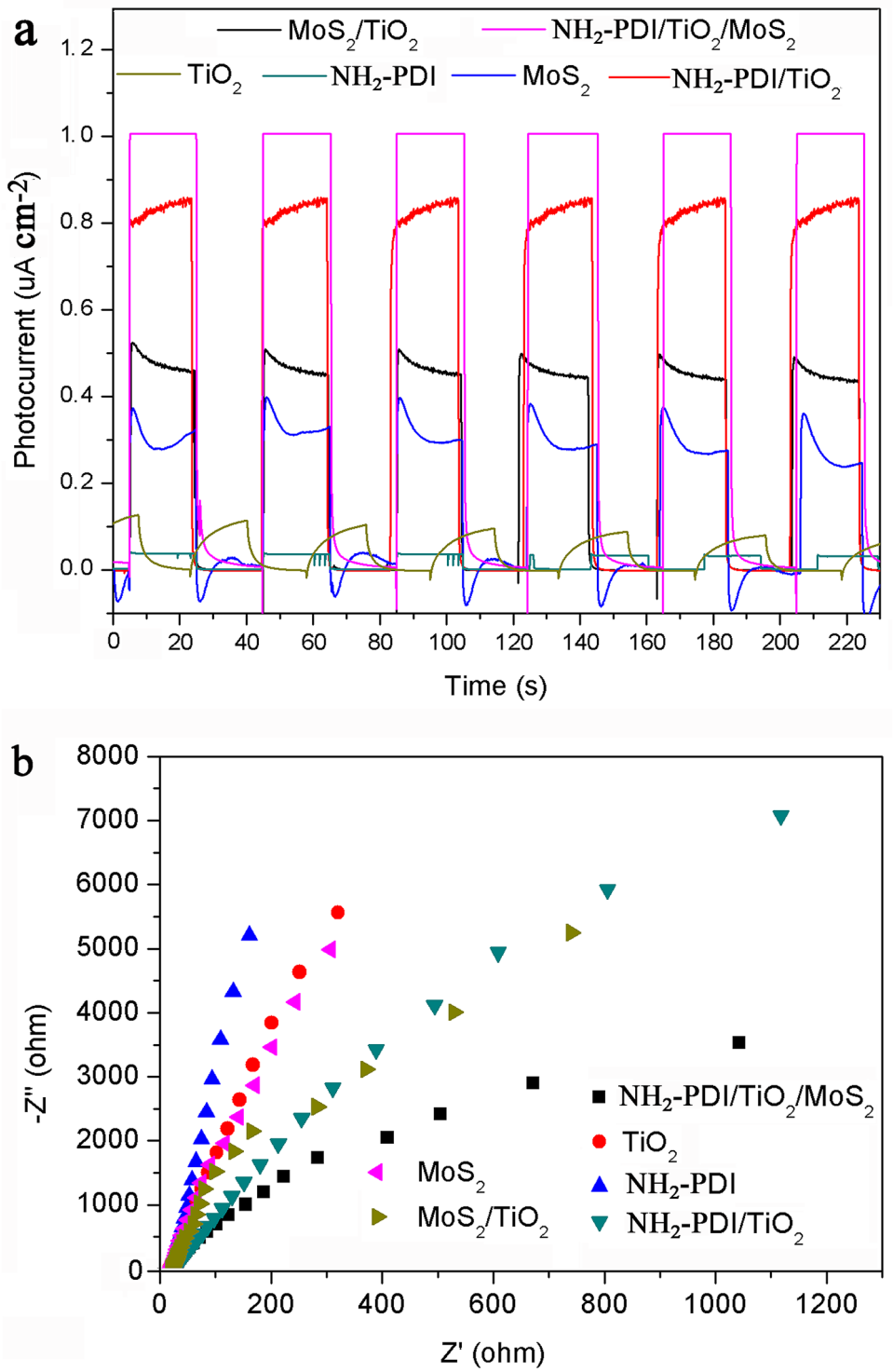

Figure 8. (**a**) Photocurrent transient responses and (**b**) EIS spectra of TiO_2, NH_2-PDI, NH_2-PDI/TiO_2, MoS_2, MoS_2/TiO_2, and NH_2-PDI/TiO_2/MoS_2 at a constant potential of 0.4 V with simulated solar light at 300 mW/cm^2. frequency: 0–10,000 Hz, electrolyte: 0.1 M Na_2SO_4, amplitude: 10 mV.

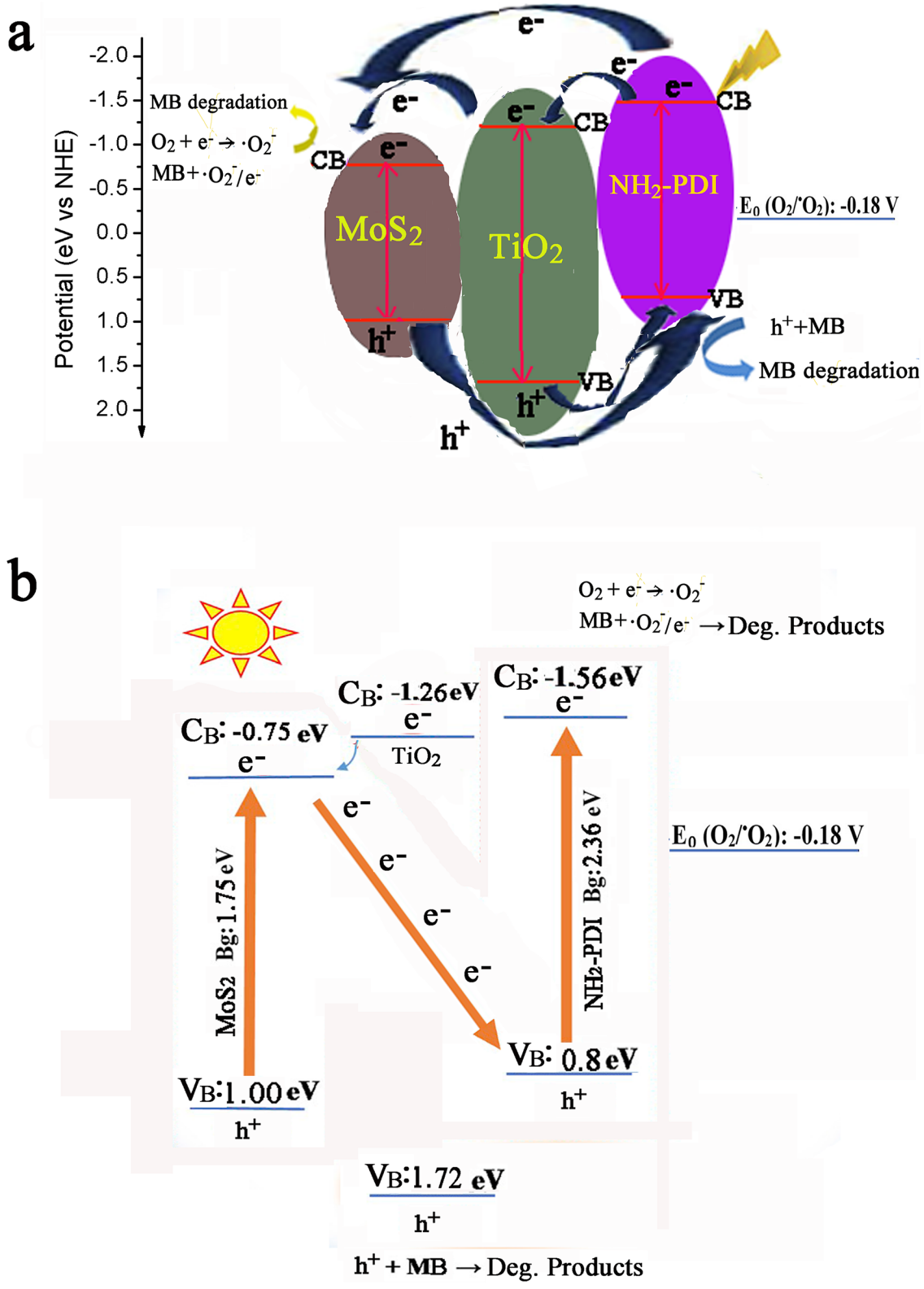

Figure 9. Schematic illustration of the photocatalytic mechanism over the NH_2-PDI/TiO_2/MoS_2 heterostructure. (**a**) Type II-Heterojunction and (**b**) Z-scheme pathways.

surface charge transfer resistance and the solid interface delamination resistance. The smaller the semicircle arc is, the easier the charge transfer proceeds[51]. Well discussion on EIS spectra and the resulted Bodes' plots has been presented in previous work[52]. Here, the following trend was obtained for the arc radius of the Nyquist plots, confirming that the NH_2-PDI/TiO_2/MoS_2 composite have better charge transfer capability.

NH_2-PDI > TiO_2 > MoS_2 > NH_2-PDI/TiO_2 > MoS_2/TiO_2 > NH_2-PDI/TiO_2/MoS_2.

The Mott-Schottky plots were used to estimate the conduction band (CB) of the TiO_2, NH_2-PDI, and MoS_2, which were − 1.26 eV, − 1.61 eV, and − 0.75 eV, respectively (Fig. S-12). Combining with their bandgaps (TiO_2 at 2.98 eV [Fig. 5b], NH_2-PDI at 2.36 eV[30], and MoS_2 at 1.75 eV[26]), the CB/VB (conduction band/valence band) of TiO_2, NH_2-PDI, and MoS_2 were evaluated to be − 1.26/1.72 eV, − 1.56/0.8 eV, and − 0.75/1.00 eV, respectively. It can be found that the CB position of singlet oxygen ($\cdot O_2^-$) (− 0.18 eV) is shallower than that of NH_2-PDI, TiO_2, and MoS_2. This result indicates that $\cdot O_2^-$ may be the main active substance in NH_2-PDI/TiO_2/MoS_2 composite for photocatalytic degradation of MB. The VB positions of MoS_2 was shallower than that of hydroxyl radical (·OH) (2.40 eV)[53], so it is possible that the ·OH cannot be generated by NH_2-PDI/TiO_2/MoS_2.

The active species in the photocatalytic process was studied by free radical capture experiment[53]. As can be seen from Fig. S-13, with the addition of p-BQ scavenger, the degradation rate decreased from 99.9% to 33%, indicating that $\cdot O_2^-$ is one of the main active species in the photocatalytic degradation process. In the presence of EDTA-2Na, the degradation efficiency was significantly reduced, indicating that h^+ is also one of the major active radicals. After the addition of IPA, the degradation activity of the catalyst did not decrease, indicating that ·OH is not the main active species in MB degradation.

Based on the results above, two mechanisms including 'type II- heterojunction' and 'Z-scheme' were suggested to illustrate the photodegradation pathways occurred in this work (Fig. 9)[54]. In 'type II- heterojunction' mechanism (Fig. 9a), both the NH_2-PDI and MoS_2 semiconductors can be excited by the arrived photons under visible light irradiation, resulting in production of e^-/h^+ pairs in both semiconductors. As the CB and VB of NH_2-PDI are located at higher energy levels than those of TiO_2 and MoS_2, the photogenerated electrons in the CB of NH_2-PDI can transfer to the CB of TiO_2, and then to the CB of MoS_2, while holes travel in the opposite direction in the VB. These charge carriers' transfer processes result in the accumulation of the photogenerated electron in the CB level of MoS_2 and the photogenerated holes in the VB level of NH_2-PDI. While in the 'Z-scheme' mechanism (Fig. 9b), the photogenerated electrons at the CB level of MoS_2 can migrate to the VB level of NH_2-PDI based on the standard potentials, and thus, the 'Z-scheme' pathway accumulates the photogenerated electrons at the CB level of NH_2-PDI and the photogenerated holes at the VB level of MoS_2. The accumulated electrons at the CB level of NH_2-PDI have the potential of − 1.61 eV, which is more negative than the potential of MoS_2 (-0.75 eV). Therefore, the accumulated electrons at the CB level of NH_2-PDI can effectively reduce dissolved oxygen and generate enough $\cdot O_2^-$ as an efficient reactive species for the degradation of MB. These holes are also stronger oxidizing agents than the accumulated holes in the VB level of NH_2-PDI (accumulated in type II mechanism) that can directly oxidize MB molecules. Therefore, the 'Z-scheme' mechanism is a better illustration for the enhanced photocatalytic activity of NH_2-PDI/TiO_2/MoS_2 composite in MB degradation than the 'type II-heterojunction' mechanism. Nevertheless, in both mechanisms, TiO_2 facilitates the electron transfer between the conduction bands, reduces photoinduced charge carrier recombination and increases photocatalytic activity.

Conclusions

In conclusion, NH_2-PDI/TiO_2/MoS_2 ternary composite was successfully synthesized by hydrothermal synthesis method. Morphological and chemical features of TiO_2, NH_2-PDI, NH_2-PDI/TiO_2, MoS_2, MoS_2/TiO_2, and NH_2-PDI/TiO_2/MoS_2 composites were examined by SEM, XRD, FTIR, XPS, and DRS. SEM results demonstrate that NH_2-PDI nanorods and MoS_2 nanoflowers mixed with TiO_2, which can provide more active sites and mass charge transport pathways in the catalytic system. The photoelectrochemical measurement results show that the photocurrent performance of the ternary composite catalyst was superior to that of binary composites or pure NH_2-PDI, MoS_2, or TiO_2. The NH_2-PDI/TiO_2/MoS_2 exhibits excellent photocatalytic activity and high stability. The 'Z-scheme' accumulates more electrons at the CB level of NH_2-PDI and photogenerated holes at the VB level of MoS_2. The accumulated electrons can effectively reduce dissolved oxygen and generate enough $\cdot O_2^-$ as an efficient reactive species for the degradation of MB. These holes are also strong oxidizing agents that can directly oxidize MB molecules. TiO_2 could reduce photoinduced charge carrier recombination and increases photocatalytic activity. This study highlights the potential application of organic and inorganic photocatalysts, and provides a feasible strategy for the photodegradation of dyes.

Received: 22 September 2020; Accepted: 30 November 2020
Published online: 15 December 2020

References

1. Nezamzadeh-Ejhieh, A. *et al.* Sunlight photodecolorization of a mixture of Methyl Orange and Bromocresol Green by CuS incorporated in a clinoptilolite zeolite as a heterogeneous catalyst. *J. Ind. Eng. Chem.* **19**, 1433–1442 (2013).
2. Tang, C. *et al.* Aerosol spray assisted assembly of TiO_2 mesocrystals into hierarchical hollow microspheres with enhanced photocatalytic performance. *Appl. Catal. B: Environ.* **201**, 41–47 (2017).
3. Testino, A. *et al.* Optimizing the photocatalytic properties of hydrothermal TiO_2 by the control of phase composition and particle morphology, A systematic approach. *J. Am. Chem. Soc.* **129**, 3564–3575 (2007).
4. Li, Y. *et al.* High efficient photocatalytic activity from nanostructuralized photonic crystal-like p-n coaxial hetero-junction film photocatalyst of Cu_3SnS_4/TiO_2 nanotube arrays. *Appl. Surf. Sci.* **426**, 770–780 (2017).
5. Wang, C. *et al.* One-pot solvothermal synthesis of carbon dots/Ag nanoparticles/TiO_2 nanocomposites with enhanced photocatalytic performance. *Ceram. Int.* **44**, 22481–22488 (2018).

6. Yan, Y. *et al.* $CuInS_2$ sensitized TiO_2 for enhanced photodegradation and hydrogen production. *Ceram. Int.* **45**, 6093–6101 (2019).
7. Gondal, M. A., Ilyas, A. M. & Baig, U. ZnO/TiO_2 nanocomposite catalyst with enhanced photovoltaic and photocatalytic performance. *Ceram. Int.* **42**, 13151–13160 (2016).
8. Ismail, A. A., Al-Sayari, S. A. & Bahnemann, D. W. Photodeposition of precious metals onto mesoporous TiO_2 nanocrystals with enhanced their photocatalytic activity for methanol oxidation. *Catal. Today* **209**, 2–7 (2013).
9. Würthner, F. Perylene bisimide dyes as versatile building blocks for functional supramolecular architectures. *Chem. Commun.* **14**, 1564–1579 (2004).
10. Gupta, R. K. & Sudhakar, A. A. Perylene based liquid crystals as materials for organic electronics applications. *Langmuir* **35**, 2455–2479 (2019).
11. Chen, K. Y. & Chow, T. J. 1, 7-Dinitroperylene bisimides: facile synthesis and characterization as n-type organic semiconductors. *Tetrahedron Lett.* **51**, 5959–5963 (2010).
12. Weitz, R. *et al.* Organic n-channel transistors based on core-cyanated perylene carboxylic diimide derivatives. *J. Am. Chem. Soc.* **130**, 4637–4645 (2008).
13. Senthilraja, A. *et al.* Self-assembly, photophysical and electrochemical properties and activation of the TiO_2 photocatalyst by perylene bisimide. *New J. Chem.* **38**, 1573–1580 (2014).
14. Chen, S. *et al.* 1D nanofiber composites of perylene diimides for visible-light-driven hydrogen evolution from water. *RSC Adv.* **4**, 48486–48491 (2014).
15. Raizada, P. *et al.* Solar photocatalytic activity of nano-ZnO supported on activated carbon or brick grain particles: role of adsorption in dye degradation. *Appl. Catal. A: Gen.* **486**, 159–169 (2014).
16. Zhang, F. *et al.* Real roles of perylene diimides for improving photocatalytic activity. *RSC Adv.* **10**, 23024–23037 (2020).
17. Li, X. *et al.* Facile synthesis of few-layered MoS_2 modified BiOI with enhanced visible-light photocatalytic activity. *Colloid Surf. A* **511**, 1–7 (2016).
18. Wu, J. M. *et al.* Piezo-catalytic effect on the enhancement of the ultra-high degradation activity in the dark by single- and fewlayers MoS_2 nanoflowers. *Adv. Mater.* **28**, 3718–3725 (2016).
19. Massey, A. T. *et al.* Hierarchical microspheres of MoS_2 nanosheets: efficient and regenerative adsorbent for removal of water-soluble dyes. *Ind. Eng. Chem. Res.* **55**, 7124–7131 (2016).
20. Song, H. J., You, S. S. & Jia, X. H. A facile in situ reduction method for the preparation of magnetic Ni/MoS_2 nanocomposites and their adsorption behaviors of congo red. *J. Mater. Sci. Mater. Electron.* **27**, 10841–10848 (2016).
21. Chen, Y. J. *et al.* Hierarchical MoS_2/Bi_2MoO_6 composites with synergistic effect for enhanced visible photocatalytic activity. *Appl. Catal. B* **164**, 40–47 (2015).
22. Hu, K. H. *et al.* The effect of morphology and size on the photocatalytic properties of MoS_2. *React. Kinet Mech. Catal.* **100**, 153–163 (2010).
23. James, D. & Zubkov, T. Photocatalytic properties of free and oxide-supported MoS_2 and WS_2 nanoparticles synthesized without surfactants. *J. Photochem. Photobiol. A* **262**, 45–51 (2013).
24. Fang, Y. Q. *et al.* Easy-separative MoS_2-glue sponges with high-efficient dye adsorption and excellent reusability for convenient water treatment. *Colloid. Surface A* **540**, 112–122 (2018).
25. Mehta, M. *et al.* Synthesis of MoS_2–TiO_2 nanocomposite for enhanced photocatalytic and photoelectrochemical performance under visible light irradiation. *Vacuum* **155**, 675–681 (2018).
26. Paul, K. *et al.* Solar light driven photoelectrocatalytic hydrogen evolution and dye degradation by metal-free few-layer MoS_2 nanoflower/TiO_2(B) nanobelts heterostructure. *Sol. Energ. Mat. Sol. C.* **185**, 364–374 (2018).
27. Du, J. *et al.* Highly efficient hydrogen evolution catalysis based on $MoS_2/CdS/TiO_2$ porous composites. *Int. J. Hydrog.* **43**, 9307–9315 (2018).
28. Azimi, S. & Nezamzadeh-Ejhieh, A. Enhanced activity of clinoptilolite-supported hybridized PbS-CdS semiconductors for the photocatalytic degradation of a mixture of tetracycline and cephalexin aqueous solution. *J. Mol. Catal. A: Chem.* **408**, 152–160 (2015).
29. Senobari, S. & Nezamzadeh-Ejhieh, A. A comprehensive study on the photocatalytic activity of coupled copper oxide-cadmium sulfide nanoparticles, *Spectrochim. Acta A: Mol. Biomol. Spect.* **196**, 334–343 (2018).
30. Chen, K. Y., Fang, T. C. & Chang, M. J. Synthesis, photophysical and electrochemical properties of 1-aminoperylene bisimides. *Dyes Pigments* **92**, 517–523 (2011).
31. Tian, L. H., Yan, X. D. & Chen, X. B. Electrochemical activity of iron phosphide nanoparticles in hydrogen evolution reaction. *ACS Catal.* **6**, 5441–5448 (2016).
32. Boom, T. V. *et al.* Charge transport in photofunctional nanoparticles self-assembled from zinc 5, 10, 15, 20-tetrakis (perylenediimide) porphyrin building blocks. *J. Am. Chem. Soc.* **124**, 9582–9590 (2002).
33. Zhang, F. Y. *et al.* Self-assembly, optical and electrical properties of perylene diimide dyes bearing unsymmetrical substituents at bay position. *Sci. Rep.* **8**, 8208–8219 (2018).
34. Miyata, T. & Masuko, T. Morphology of poly (l-lactide) solution-grown crystals. *Polymer* **38**, 4003–4009 (1997).
35. Ohsaka, T. & Fujiki, Y. Raman spectra in hollandite type compounds. *Solid State Commun.* **44**, 1325–1327 (1982).
36. Abbad, M. B. *et al.* Synthesis and catalytic activity of TiO_2 nanoparticles for photochemical oxidation of concentrated chlorophenols under direct solar radiation. *Int. J. Electrochem. Sci.* **7**, 4871–4888 (2012).
37. Tamiji, T. & Nezamzadeh-Ejhieh, A. Study of kinetics aspects of the electrocatalytic oxidation of benzyl alcohol in aqueous solution on AgBr modified carbon paste electrode. *Mater. Chem. Phys.* **237**, 121813 (2019).
38. Virsek, M. *et al.* Raman scattering of the MoS_2 and WS_2 single nanotubes. *J. Surf. Sci.* **601**, 2868–2872 (2007).
39. Wang, L. *et al.* Ag_3PO_4 nanoparticles loaded on 3D flower-like spherical MoS_2: highly efficient hierarchical heterojunction photocatalyst. *Dalton Trans.* **44**, 14625–14634 (2015).
40. Kai, L. *et al.* In-situ-reduced synthesis of Ti^{3+} self-doped TiO_2/g-C_3N_4 heterojunctions with high photocatalytic performance under LED light irradiation. *ACS Appl. Mater. Inter.* **7**, 9023–9030 (2015).
41. Zhang, W. W. *et al.* Constructing ternary polyaniline-graphene-TiO_2 hybrids with enhanced photoelectrochemical performance in photogenerated cathodic protection. *Appl. Surf. Sci.* **410**, 547–556 (2017).
42. Wang, P. *et al.* Dye-sensitization induced visible-light reduction of graphene oxide for the enhanced TiO_2 photocatalytic performance. *ACS Appl. Mater. Inter.* **5**, 2924–2929 (2013).
43. Yuan, Y. *et al.* Constructing anatase TiO_2 nanosheets with exposed (001) facets/layered MoS_2 two-dimensional nanojunctions for enhanced solar hydrogen generation. *ACS Catal.* **6**, 532–541 (2016).
44. Eshaghi, A. *et al.* Optical and photocatalytic properties of the Fe-doped TiO_2 nanoparticles loaded on the activated carbon. *Adv. Powder Technol.* **29**, 1879–1885 (2018).
45. Mirsalari, S. A. *et al.* The catalytic activity of the coupled CdS-AgBr nanoparticles: a brief study on characterization and its photodecolorization activity towards methylene blue. *Desal. Water Treat.* **175**, 263–272 (2020).
46. Velmurugan, R. *et al.* Preparation and characterization of carbon nanoparticles loaded TiO_2 and its catalytic activity driven by natural sunlight. *Sol. Energ. Mat. Sol. C.* **108**, 205–212 (2013).
47. Tian, J. *et al.* Enhanced photocatalytic performances of CeO_2/TiO_2 nanobelt heterostructures. *Small* **9**, 3864–3872 (2013).
48. Nosuhi, M. & Nezamzadeh-Ejhieh, A. High catalytic activity of Fe(II)-clinoptilolite nanoparticales for indirect voltammetric determination of dichromate: Experimental design by response surface methodology (RSM). *Electrochim. Acta* **223**, 47–62 (2017).

49. Derikvandi, H. & Nezamzadeh-Ejhieh, A. A comprehensive study on electrochemical and photocatalytic activity of SnO_2-ZnO/clinoptilolite nanoparticles. *J. Molecul. Catal. A: Chem.* **426**, 158–169 (2017).
50. Ma, Y. *et al.* Self assembly, optical and electrical properties of five membered O- or S-heterocyclic annulated perylene diimides. *Dyes Pigments* **135**, 41–48 (2016).
51. Ghattavi, S. *et al.* A visible light driven AgBr/g-C3N4 photocatalyst composite in methyl orange photodegradation: Focus on photoluminescence, mole ratio, synthesis method of g-C_3N_4 and scavengers. *Compos. B* **183**, 107712 (2020).
52. Omrani, N. *et al.* A comprehensive study on the mechanism pathways and scavenging agents in the photocatalytic activity of $BiVO_4$/WO_3 nano-composite. *J. Water Proc. Eng.* **33**, 101094 (2020).
53. Senobaria, S. & Nezamzadeh-Ejhieh, A. A p-n junction NiO-CdS nanoparticles with enhanced photocatalytic activity: a response surface methodology study. *J. Mol. Liq.* **257**, 173–183 (2018).
54. Lu, D. *et al.* Highly efficient visible-light-induced photoactivity of Z-scheme g-C_3N_4/Ag/MoS_2 ternary photocatalysts for organic pollutant degradation and production of hydrogen. *ACS Sustain. Chem. Eng.* **5**, 1436–1445 (2017).

Acknowledgements

This work was supported by the Doctoral Research Fund of Shandong Jianzhu University (XNBS1712, XNBS1938), Science and Technology Plan Project of Housing and Urban-Rural Construction Department in Shandong Province (2018-K11-01), and Youth Innovation Technology Project of Higher School in Shandong Province (2019KJD003).

Author contributions

Guarantor of integrity of entire study—Y.M. Study concepts—Y.M.Study design—Y.M. Literature research—F.Z. experimental studies—F.Z. Data acquisition—Y.W. Data analysis/interpretation—F.Z.Statistical analysis—T.J. Manuscript preparation—Y.M. Manuscript definition of intellectual content—Y.M. Manuscript editing—X.L.Manuscript revision/review—Y.Z. Manuscript fnal version approval—Y.M.

Competing interests

The authors declare no competing interests.

Additional information

Supplementary Information The online version contains supplementary material available at https://doi.org/10.1038/s41598-020-78894-y.

Correspondence and requests for materials should be addressed to Y.M. or F.Z.

Reprints and permissions information is available at www.nature.com/reprints.

Publisher's note Springer Nature remains neutral with regard to jurisdictional claims in published maps and institutional affiliations.